applied sciences

MDPI

Article

Multipoint Thermal Sensing System for Power Semiconductor Devices Utilizing Fiber Bragg Gratings

Ridwanullahi Isa [1,2], Naveed Iqbal [2,3], Mohammad Abido [2], Jawad Mirza [4,5] and Khurram Karim Qureshi [1,3,*]

1 Optical Communications and Sensors Laboratory (OCSL), Electrical Engineering Department, King Fahd University of Petroleum and Minerals, Dhahran 31261, Saudi Arabia; g202110270@kfupm.edu.sa
2 Electrical Engineering Department, King Fahd University of Petroleum and Minerals, Dhahran 31261, Saudi Arabia; naveediqbal@kfupm.edu.sa (N.I.); mabido@kfupm.edu.sa (M.A.)
3 Center for Communication Systems and Sensing, King Fahd University of Petroleum and Minerals, Dhahran 31261, Saudi Arabia
4 SEECS Photonic Research Group, Islamabad 44000, Pakistan; 15phdee001@hitecuni.edu.pk
5 Department of Electrical Engineering, Hitec University, Taxila 47080, Pakistan
* Correspondence: kqureshi@kfupm.edu.sa

Abstract: This study investigates the feasibility of using fiber Bragg grating (FBG) sensors for multipoint thermal monitoring of several power semiconductor devices (PSDs), such as insulated gate bipolar transistors (IGBTs), and rectifiers assembled on a common heatsink in a three-phase inverter. A novel approach is proposed to integrate FBG sensors beneath the baseplates of the IGBT modules, avoiding the need for invasive modifications to the device structure. By strategically positioning multiple FBG sensors, accurate temperature profiles of critical components can be obtained. The experimental results demonstrate the effectiveness of the proposed method, with the temperature measurements from FBG sensors closely matching those obtained using thermal infrared (IR) cameras within ±1.1 °C. This research highlights the potential of FBG sensors for reliable and precise thermal management in power electronic systems, contributing to improved performance and reliability.

Keywords: fiber optic sensors; power electronics; IGBT; junction temperature; multipoint sensing

Citation: Isa, R.; Iqbal, N.; Abido, M.; Mirza, J.; Qureshi, K.K. Multipoint Thermal Sensing System for Power Semiconductor Devices Utilizing Fiber Bragg Gratings. *Appl. Sci.* **2024**, *14*, 11328. https://doi.org/10.3390/app142311328

Academic Editors: Detlef Kip, Uma Maheswari Rajagopalan and Yoshikazu Koike

Received: 18 October 2024
Revised: 21 November 2024
Accepted: 2 December 2024
Published: 4 December 2024

1. Introduction

Power electronic systems have found widespread applications in various fields, including hybrid electric vehicles and renewable energy systems [1,2]. These systems are driven by a variety of power semiconductor devices (PSDs), such as IGBTs and silicon carbide semiconductor field effect transistors (SiC-MOSFETs) [3]. In high-power applications where circuit robustness is required, multiple IGBTs are used to control the electrical current in the circuit [4]. As such, the adoption of IGBTs continues to grow as power systems evolve and advance. However, one of the major causes of failure is the high operating temperature within the chip due to thermal cycling [5–7]. Typically, power systems that exploit IGBTs in their circuitry are likely to experience variations in the electrical input signal, the terminal load, and the switching frequency, where these varying parameters contribute to the increase in IGBTs' junction temperature (T_j) [8]. This in turn accelerates the wear-out and degrades the overall performance and reliability of IGBTs [9,10]. To prevent overburdening the IGBTs with thermal stress, several studies have reported numerous techniques for monitoring the junction temperature [11–14].

There are two methods for determining the junction temperature, i.e., electrical- and optical-based techniques. The estimation based on electrical techniques includes temperature-sensitive electrical parameters (TSEPs) [12,15] and temperature-sensitive electrical devices (TSEDs) [13,16]. TSEP techniques rely on electrical parameters, such as turn-off delay [17], collector–emitter voltage [18], and on-state resistance [19], to estimate

T_j. Since these parameters can vary with the age of the IGBT, they may not always be reliable for T_j estimation. On the other hand, the TSED technique uses electrical devices and components like silicon diodes [20], thermistors, and thermocouples [13], which are prone to measurement errors due to thermal contact resistance.

The optical methods include temperature-sensitive optical parameters (TSOPs), infrared cameras (IRCs), and the fiber Bragg grating (FBG) technology [16]. TSOPs use the electroluminescence of forward bias silicon devices to estimate T_j [21], yet this method is not useful for commercial IGBTs. An IRC, being involved in the most common optical method, is used in various fields [22] and renders a visual 2D display of the surface temperature distribution. However, it necessitates direct line-of-sight and homogeneity of the targeted surface. On the other hand, the FBG sensing technique offers a unique advantage for T_j sensing due to its miniaturization, immunity to electromagnetic interference, inherent robustness, and multiplexing capability.

The multiplexing feature enables the implementation of T_j sensing for multiple devices as opposed to other techniques confined to single-point measurement. Previous studies on FBG techniques have explored the direct placement of sensors on the IGBT's chip or affixed to the bond wires, or forming a groove at a surface of the structure or baseplate [23–27]. Unfortunately, this arrangement is limited by the encapsulation of the IGBT as it requires dismantling the ceramic casing. Moreover, it is difficult for commercial application and may also affect the thermal distribution and aging of the device or cutting due to altercations in the device's structure.

To address these challenges, this paper introduces a multipoint thermal sensing approach utilizing three FBG sensors with distinct wavelengths. These sensors were positioned beneath two IGBTs and a packed rectifier baseplate installed on a common heatsink in a three-phase inverter without a groove at the surface of the baseplate. The study examines the performance of both single-point and multipoint sensing capabilities of FBG sensors using a single optical fiber. The underlying goal of this study is to investigate the practical utility and optimum placement of FBG sensors for in situ thermal monitoring and thermal profiling of power electronics systems, extending beyond mere laboratory demonstrations. The detailed installation methods facilitate the easy and effective implementation of the FBG-based sensing technique for commercial applications.

2. FBG Temperature Sensing Principle

FBGs are composed of an optical fiber inscribed with gratings to selectively reflect light at specific wavelengths. For precision and versatility, the phase mask technique is the common method of fabricating FBG sensors. This is achieved by placing a phase mask with a finely etched diffraction grating of period Λ directly along the length of the optical fiber where gratings are desired. The phase mask, which is aligned with the fiber, diffracts the UV beam emitted from the excimer laser into several orders, creating an interference pattern in the form of fringes along the fiber core. These fringes modulate the refractive index of the fiber core periodically, creating the Bragg grating [28]. For sensing applications, the light beam propagating through the optical fiber is reflected by the inscribed gratings at the central Bragg wavelength λ_B, which is a function of the effective refractive index of the fiber core n_{eff}. The Bragg wavelength is expressed as

$$\lambda_B = 2\, n_{eff}\, \Lambda \tag{1}$$

when the grating portion is subjected to mechanical and thermal stress. The periodicity and the effective index of the core changes, which causes central wavelength shift $\Delta\lambda_B$ in proportion to the stress experienced, expressed as

$$\frac{\Delta\lambda_B}{\lambda_B} = \left(\alpha_f + \xi\right)\Delta T + (1 - p_{eff})\Delta\varepsilon \tag{2}$$

where ΔT and $\Delta\varepsilon$ are the change in temperature and mechanical stress, respectively, α_f and ξ are the fiber thermal expansion and thermo-optic coefficients, while p_{eff} is the fiber photo-elastic parameter. Given that the effect of strain on the FBG sensor is uniform, the Bragg wavelength shift $\Delta\lambda_B$ is reduced to

$$\frac{\Delta\lambda_B}{\lambda_B} = \left(a_f + \xi\right)\Delta T \tag{3}$$

2.1. Heat Transfer Model

In [2], it is assumed that the mechanical stress remains constant throughout the distributed sensitive portion of the FBG sensors. Similarly, this work will adhere to that assumption, ensuring that the reflected wavelength depends solely on the thermal variations along the length of the sensor head. In this research, we employed a three-phase inverter (from SEMIKRON corporation), a renowned manufacturer of power semiconductor devices, including IGBTs, to investigate multipoint temperature sensing for IGBTs in the inverter. The inverter is a multifunctional three-phase inverter with a six-diode packed rectifier and IGBT modules, suitable for different converter configurations, as detailed in Figure 1.

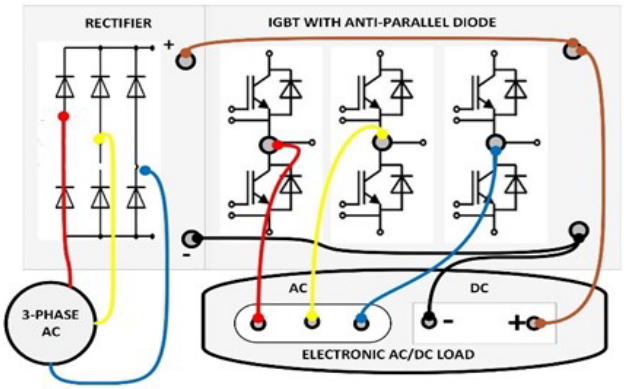

Figure 1. Schematic of a three-phase inverter.

The heat transfer through the IGBT layers to the sensor interface was modeled to evaluate the thermal behavior of the PSDs arranged on the heatsink. Here, the heat transfer equation for an IGBT module is derived for the direct on-chip sensor placement, the outer casing, and the heatsink. Subsequently, the model is extended to include multiple semiconductor devices, including two IGBTs, and a rectifier module to achieve multipoint temperature measurement.

2.1.1. Single-Point Model

For a discrete IGBT module with direct on-chip sensor placement, a simplified static thermal resistance model can be used to estimate heat transfer across the chip-to-sensor interface. In this case of the IGBT–FBG sensor interface, we neglect the coupling effect between the switches; therefore, we can estimate the junction temperature with the thermal resistance network provided that the sensor is held very close to the IGBT's chip and assuming that the measurement is completed in an enclosure with an ambient temperature T_a. The general expression for T_j is provided by

$$T_j = \left[P_{di}R_{th(j-a)}\right] + T_a \tag{4}$$

where P_{di} is the allowable dissipated power across the device; $R_{th(j-a)}$ is the junction-to-ambient thermal resistance.

In this study, the sensor is placed between the IGBT's baseplate and the heatsink. Thus, we can modify (4) to capture the heat loss across the various layers of the module.

As shown in Figure 2, the MOSFETs and IGBTs used in high-power applications typically have an additional diode in parallel to provide a reverse current path for inductive loads. The corresponding junction-to-case thermal resistance for such a module $R_{eq(j-c)}$ can be expressed as an equivalent sum of the anti-parallel diode and IGBT as

$$R_{eq(j-c)} = \frac{\left(R_{th(j-c)I}\, R_{th(j-c)D}\right)}{\left(R_{th(j-c)I} + R_{th(j-c)D}\right)} \tag{5}$$

where $R_{th(j-c)I}$ and $R_{th(j-c)D}$ are the thermal resistance for anti-parallel diode and IGBT, respectively. Typically, $R_{eq(j-c)}$ and $R_{th(c-h)}$ are specified by the manufacturer. Generally, $R_{th(c-h)}$ can be merely estimated as a function of thermal conductivity of the used thermal pad through the following relation.

$$R_{th(c-h)} = \frac{T}{kA} \tag{6}$$

where T is the thickness of the interface layer between the module and the heatsink, A represents the area occupied by thermal paste, and k is the specified thermal conductivity of the material. The equivalent thermal resistance for junction-to-ambient $R_{th(j-a)}$ is a sum of $R_{eq(j-h)}$ and $R_{eq(j-a)}$, which are the thermal resistance for junction-to-heatsink and junction-to-ambient, provided as

$$R_{eq(j-h)} = R_{eq(j-c)} + R_{eq(c-h)} \tag{7}$$

$$R_{th(j-a)} = R_{eq(j-h)} + R_{th(h-a)} \tag{8}$$

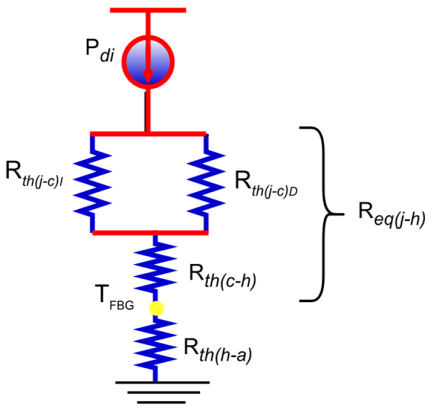

Figure 2. Thermal network of a single IGBT module referenced to FBG sensor.

The estimated junction temperature for a point measurement with reference to the measured temperature of FBG T_{FBG} attached to the IGBT baseplate is provided as

$$T_j = \left(R_{eq(j-c)} + R_{th(c-h)} + R_{th(h-a)}\right) P_{di} + T_{FBG} \tag{9}$$

where $R_{th(c-h)}$ is the thermal resistance of the device's casing-to-heatsink. Thus, the relationship for the thermal resistance heatsink-to-ambient can be expressed as

$$R_{th(h-a)} = \frac{T_j - T_{FBG}}{P_{di}} - \left(R_{th(j-c)} + R_{th(c-h)}\right) \tag{10}$$

2.1.2. Multipoint Model

As depicted in Figure 3, a typical inverter circuit consists of three or more PSDs mounted on a heatsink. These devices encompass IGBTs, SiC MOSFETs, or rectifier modules.

In order to monitor the temperature variations regarding these devices, multipoint sensors are required. Installing a standalone sensor for each device would not be economical and eventually make the circuit bulky. Similar to the single-point model, the approach for static thermal network resistance measurement is valid for three-phase inverters if all IGBTs are assumed to experience the same loss, except in the case of a half-bridge operating as a bulk converter [26].

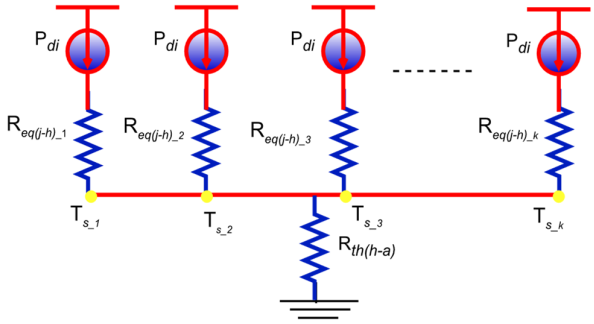

Figure 3. Thermal resistance network of multiple IGBTs.

To estimate the mean junction temperature of multiple PSDs mounted on a common heatsink, a thermal resistance network model is employed. This model simplifies the complex thermal behavior of the system into a series and parallel combination of thermal resistances. By considering the thermal resistances of the individual components, including the junction-to-case, case-to-heatsink, and heatsink-to-ambient resistances, the overall thermal resistance between the junction and the ambient is calculated. The mean junction temperature is then determined by considering the total power dissipation, the equivalent thermal resistance, and the average heatsink temperature. This approach provides a valuable tool for thermal management and reliability analysis of power electronic systems [29].

Suppose the sensors are located on the IGBT chips along a fiber cable, where the cable functions as a continuous sensor that can identify temperature changes at each discrete sensing point, and then the equivalent value of T_j for these devices is provided as

$$T_j = \left[P_{di} R_{th(j-a)}\right] n + T_a \tag{11}$$

where n is the number of PSDs mounted on the heatsink; $R_{th(j-h)}$ and P_{di} are, respectively, the thermal resistance and the sum of power dissipation in each PSD.

Now, if the FBG sensor is positioned outside the device's housing to measure T_j of a packed rectifier, the equivalent junction-to-case thermal resistance $R_{eq(j-c)R}$ of the rectifier is expressed as

$$R_{eq(j-c)R} = \left[\frac{1}{R_{D1}} + \frac{1}{R_{D2}} + \frac{1}{R_{D3}} \ldots\ldots\ldots\ldots \frac{1}{R_{DN}}\right]^{-1} \tag{12}$$

where R_{D1} to R_{DN} represent the parallel combination of the N diodes used for rectification. For an isolated system, the casing temperature for the rectifier stud $T_{c(R)}$ is a function of the P_{di} in the rectifier stud and $R_{eq(j-c)R}$ and is expressed as

$$T_{c(R)} = P_{di}\, R_{eq(j-c)R} \tag{13}$$

The thermal resistance junction-to-heatsink for any kth device $R_{th(j-h)\_k}$ is provided as

$$R_{th(j-h)\_k} = \left[\frac{T_{j-k} - T_{s-k}}{P_{di} N} - R_{th(j-c)}\right] + R_{th(c-h)} \tag{14}$$

where N represents the number of separate semiconductors contained within the module stacked onto the heatsink. A three-phase bridge situated on the heatsink, which contains six diodes packed onto a single stud, will simply have n = 1 and N = 6 for brevity. The overall dissipated power on the heatsink equates to $P_{di} * N$. Thus, the estimated junction temperature T_{j_k} for the kth device module referenced to the temperate sensor is provided as

$$T_{j-k} = P_{di} R_{eq(j-h)\_k} + T_{s\_k} \quad (15)$$

The equivalent $R_{eq(j-h)}$ for all the modules, i.e., $R_{eq(j-h)\_1}$, $R_{eq(j-h)\_2}$, … $R_{eq(j-h)\_k}$, is parallel combination of all the modules on the heatsink and is provided as

$$R_{eq(j-h)} = \left[\frac{1}{R_{eq(j-h)\_1}} + \frac{1}{R_{eq(j-h)\_2}} + \ldots \frac{1}{R_{eq(j-h)\_k}} \right]^{-1} \quad (16)$$

while the expression for the equivalent $R_{th(j-a)}$ is provided as

$$R_{th(j-a)} = \left[\left(R_{eq(j-h)}\right) n_R + \left(R_{eq(j-h)}\right) n_I \ldots\ldots + \left(R_{eq(j-h)}\right) n_o \right] + R_{th(h-a)} \quad (17)$$

where $R_{eq(j-h)n_o}$ represents the thermal resistance of junction-to-heatsink for other PSS devices mounted on the heatsink; n_R, n_I, and n_o represent the number of rectifiers, IGBT modules, and other PSS devices stacked on the heatsink, respectively. Considering the equivalent sum of P_{di} at each semiconductor module, the mean junction temperature for all the semiconductors combined on a heatsink, $T_{j(mean)}$, is provided as

$$T_{j(mean)} = \left[\frac{P_{di} R_{th(j-a)}}{F} \right] + T_{s\_mean} \quad (18)$$

where F is the safety factor for operation temperature. To avoid using devices beyond the maximum allowable temperature, the manufacturers typically recommend a safety factor of 0.85 [30].

3. Sensors' Calibration and Installation

This section describes the practical installation procedures for the FBG sensors utilized in this study. The temperature–wavelength ($T - \lambda$) relationship was measured both before and after integrating the sensors into the SEMIKRON inverter. This is necessary to obtain the sensitivity of the sensor, and to determine whether the proposed installation meets the requirement for onsite calibration. In addition, the performance of the sensors was examined in different installation configurations. The details of the FBG sensors and the process of installation are discussed in the following subsection.

3.1. Calibration of FBG Sensors

Firstly, an FBG sensor (FBG1) with a central Bragg wavelength of 1530 nm was affixed to a stainless-steel plate and placed within a digitally controlled heater. A broadband light source (BBS) was utilized to transmit light through the optical fiber sensor placed on the pre-heater, as depicted in Figure 4, for calibration purposes. The optical light generated at 100 mW is transmitted via the optical circulator to the FBG sensor positioned on the heater, and the reflected signal is then redirected through the circulator to the optical spectrum analyzer for visual display of wavelength. To minimize the impact of fluctuating room temperatures, the setup was isolated within a transparent glass enclosure.

The digital control heater regulated the temperature within a range of 30 to 100 °C, maintaining a constant 10 °C increment. The FBG sensors used in this study had a head length of approximately 5 mm. The choice of 5 mm FBG sensors was based on a balance between spatial resolution and ease of installation. Shorter sensors (e.g., 1 mm) can provide higher resolution but are more sensitive to placement and external disturbances. However, longer sensors (e.g., 5 mm) offer better robustness and easier installation, making

them suitable for larger areas with fewer critical spatial resolution requirements [23]. Considering the IGBT baseplate's surface area and the need to capture significant temperature variations, 5 mm FBG sensors were deemed to be the optimal choice in this work. The Bragg wavelength at each temperature level was measured using a spectrum analyzer with a resolution of 0.01 nm, and the resulting temperature–wavelength curve is illustrated in Figure 5. The sensitivity of FBG1 was roughly 8.94 pm/°C, with a correlation coefficient R^2 of 0.999 using a second-order polynomial fit, and the measurement was conducted at three different times for the sake of repeatability. This process is replicated with two other sensors, i.e., FBG2 and FBG3, at the center wavelengths of 1540 nm and 1555 nm, and the resulting sensitivities were approximately 9.09 pm/°C and 9.89 pm/°C, respectively.

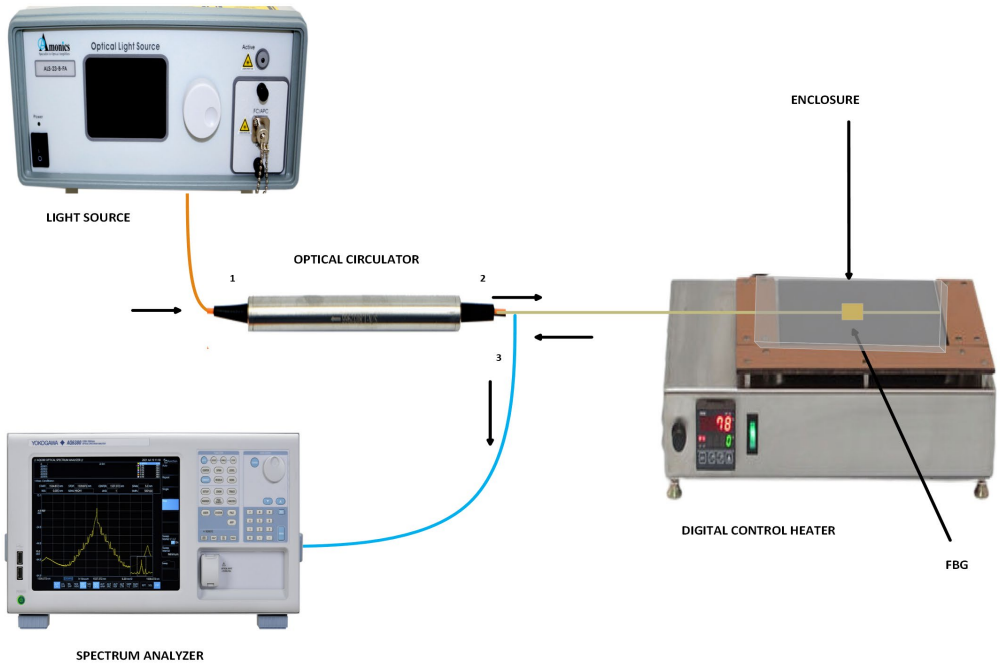

Figure 4. Schematic of the calibration setup.

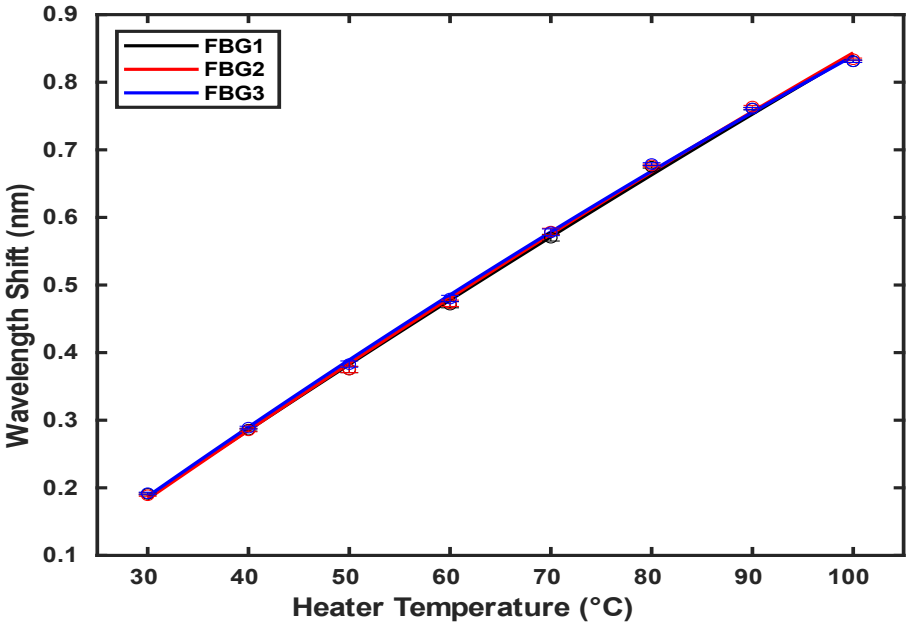

Figure 5. Temperature–wavelength correlation of FBG sensors.

3.2. FBG Sensors Installation

In this setup, the FBG sensor was placed between the copper plate and the heatsink, unlike the method used in [31], where the sensors are placed directly on the IGBT chips. The direct method is exclusively meant for experimental purposes because of the necessity to break the ceramic casing embedding the IGBT chips, which is not suitable for commercial applications. For this approach, it is unnecessary to remove the housing of the IGBTs in order to place the sensor for junction temperature measurements. Instead, the expressions in (9) and (14) can be combined to estimate T_j.

The three FBG sensors (FBG1, FBG2, and FBG3) are connected in a series arrangement, as shown in Figure 6a, to form a single fiber. The inverter utilized in this experiment comprises four IGBT studs and a sole three-phase rectifier stud stacked on the heatsink. As depicted in Figure 6b, two of the IGBTs, together with the rectifier module, have been selected for this experiment. For the installation of the fiber sensor, the rectifier and IGBT studs were loosened off the heatsink, and the fiber sensor was laid out and examined for the two different configurations shown in Figure 6c,d.

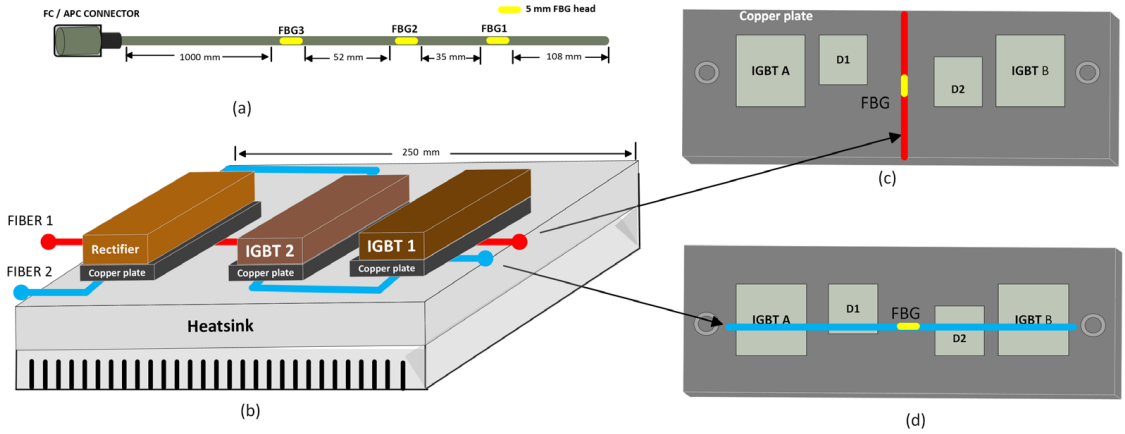

Figure 6. (**a**) FBG array in a single optical fiber. (**b**) Installation settings of the sensors in the inverter circuit (**c**) FIBER1; vertical sensor configuration along the rectifier/IGBT baseplate. (**d**) FIBER2; horizontal sensor configuration along the rectifier/IGBTs baseplate.

In the first arrangement (FIBER1), the fiber was laid beneath the module's plate across the two parallel IGBTs and diode chips, cutting through the plate vertically, as shown in Figure 6c. However, the second setup (FIBER2) involved positioning the fiber parallel to the plate and cutting through the module's plate horizontally, as illustrated in Figure 6d. To obtain precise measurement results, we positioned the sensor heads at the midpoint of the IGBT plate for both setups, following the location guidelines proposed in [22]. The IGBTs were then mounted to the heatsink, ensuring that the torque was maintained under an acceptable limit to avoid undue stress that may cause damage to the fiber. The experimental results for the two installations are discussed in the next section.

4. Experimental Setup

FBG Array Installation and Multiplexing

The inverter circuit was powered by a three-phase AC supply to drive the electronic load, which increased the IGBT's temperature by exposing the FBG array sensors to different types of static thermal stresses. The FBG sensors are placed between the IGBT baseplate and the heatsink inside the inverter. Post-installation calibration of the sensor is necessary to ensure that the Bragg wavelength recorded during the air–interface calibration as shown in Figure 5 is maintained for the IGBT–FBG interface. Initially, we utilized the installation setting (FIBER1) depicted in Figure 6c.

After the sensors were calibrated, the fiber was threaded through the transparent inverter's housing opening to the IGBTs. Figure 7a shows the tabletop experimental setup,

where the FBG port is attached to the inverter's plastic casing for ease of connection and disconnection. To determine the optimal placement for thermal sensing, the performance of the two setups (FIBER1 and FIBER2) was compared. The Bragg wavelength at varying temperatures was recorded and validated using measurements from an IR thermal camera (FLIR E53) positioned 10 cm away from the baseplate of the invertor.

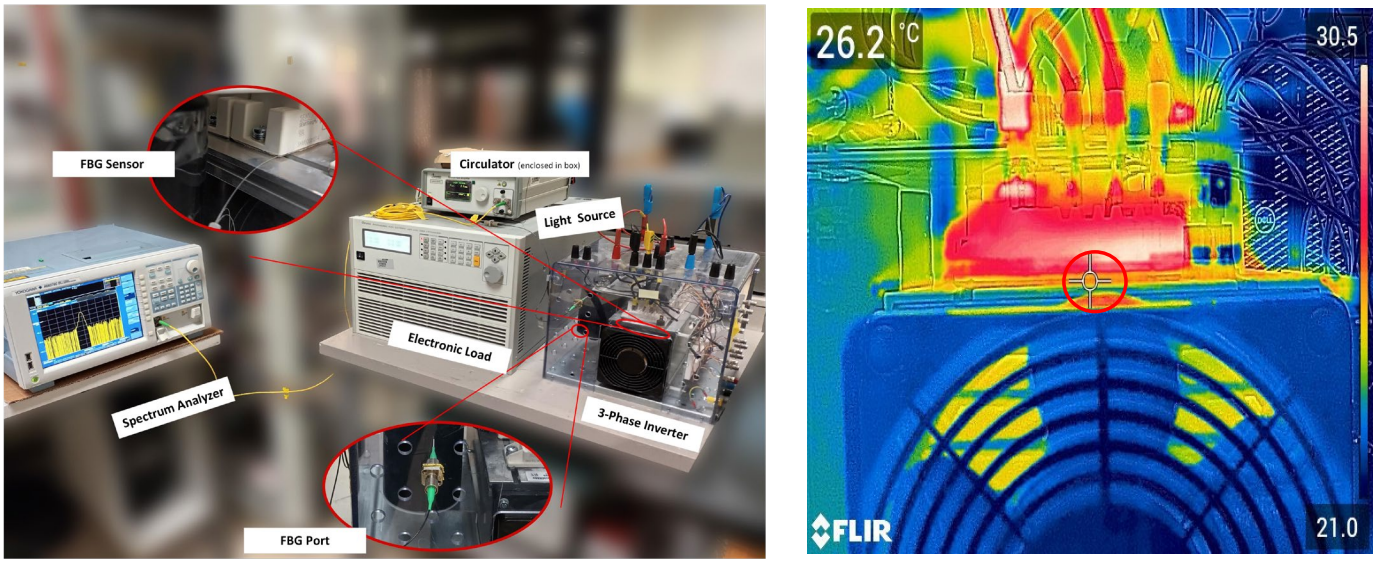

(**a**) (**b**)

Figure 7. (**a**) Tabletop experimental setup. (**b**) Thermal imaging of the IGBT.

As shown in Figure 7b, the red circle at the center indicates the specific location where the IR camera measurement was taken, corresponding to the position of the FBG sensor. This visual representation shows the spatial alignment between the two measurement techniques. The IR camera imaged the surface temperature of 26.2 °C along the baseplate, which corresponds to an average temperature value of 25.51 °C for FBG1, estimated based on the observed reflected wavelength on the optical spectrum analyzer for three different measurements. The same process was repeated for the FIBER2 configuration. In both configurations, it is apparent that the three FBGs have good linearity, with an R^2 value of greater than 0.999. Table 1 presents the estimated parameters for the second-order polynomial fit curves and the mean squared error (MSE) of the sensors at the ambient temperature of 21.9 °C.

Table 1. Fitting curve parameters for fiber configurations.

Settings	FIBER1				FIBER2			
	Intercept	Ambient Temp. (°C)	MSE	R^2	Intercept	MSE	R^2	Ambient Temp. (°C)
FBG1	1529.7	21.9	0.00628	0.9997	1529.7	0.00679	0.9996	21.9
FBG2	1539.85	21.9	0.00329	0.9999	1539.86	0.00321	0.9999	21.9
FBG3	1555.04	21.9	0.0044	0.9999	1555.01	0.00497	0.9998	21.9

The three sensors, namely FBG1, FBG2, and FBG3, exhibit sensitivities of 9.1, 9.3, and 9.93 pm/°C, respectively. The maximum sensitivity shift reported is roughly 2 pm. A slight deviation in sensor sensitivity was observed compared to pre-installation calibration, likely due to strain induced on the FBG sensor when sandwiched between the copper baseplate and heatsink.

5. Results and Discussion

5.1. Load Power vs. IGBT Temperature

Having established the sensitivity of the FBG array after its installation, since both fiber configurations (vertical and horizontal) for FIBER1 and FIBER2 exhibit similar characteristics, we chose the vertical orientation (FIBER1) for our experiment. This choice was made to simplify the installation and minimize the risk of fiber damage that could occur if the fiber were to cross or block the hole used for tightening the IGBT baseplate to the heatsink. In this work, the electronic load "Chroma 63802" was set to constant power mode since we were interested in monitoring the temperature of PSDs with respect to the input load. Due to equipment limitations, the load power P_L was adjusted with 0.5 kW intervals from 0 to 4 kW. When the load power is applied to the inverter, the current changes, while the power and conduction losses cause the temperature of the IGBT modules to increase. For the values of P_L presented in Table 2, the temperature gradient measured by the three sensors, T_{FBG1}, T_{FBG2}, and T_{FBG3}, along the IGBT baseplate was estimated using the average Bragg wavelength demodulated from the optical spectrum analyzer. Each measurement was repeated three times for each load power P_L to ensure accuracy.

Table 2. Temperature measurements for IGBTs at constant P_L.

Load Power P_L (kW)	Temperature (°C)								
	T_{FBG1}	T_{IR}	T_{DIF}	T_{FBG2}	T_{IR}	T_{DIF}	T_{FBG3}	T_{IR}	T_{DIF}
0	22.10	22.1	0.00	22.8	22.8	0.00	22.60	22.6	0.00
0.5	25.51	26.2	0.69	27.68	27.8	0.12	25.24	24.6	0.64
1	28.93	29.0	0.07	31.33	31.5	0.17	27.01	26.9	0.11
1.5	33.49	34.3	0.79	34.85	34.6	0.25	28.55	29.5	0.95
2	38.32	38.2	0.12	37.50	37.4	0.10	33.18	33.5	0.32
2.5	44.44	44.9	0.46	41.02	40.6	0.42	36.71	36.5	0.21
3	48.2	48.56	0.36	44.55	45.2	0.65	39.35	39.5	0.15
3.5	53.2	53.68	0.48	50.72	50.5	0.22	40.89	41.4	0.51
4	56.84	57.85	1.1	55.8	56.2	0.4	43.76	44.2	0.44

As mentioned in Section 3.1, the center wavelengths for FBG1, FBG2, and FBG3 in this experiment are 1530 nm, 1540 nm, and 1555 nm, respectively. Due to equipment limitations, only two FBG spectra can be displayed on the OSA at a time. Therefore, the measurement from the third FBG is obtained by resetting the OSA to the corresponding central wavelength and viewing it at the upper or lower half of the screen. As shown in Figure 8, the Bragg wavelengths correspond to each peak at the upper and lower windows on the OSA. The calculated wavelength shifts between the present and reference measurements are then translated into temperature changes. The wavelength varies depending on the temperature sensed by the FBG sensor at the baseplate of each module, while T_{IR} is the average surface temperature sensed by the thermal camera for the respective IGBT/rectifier along the baseplate. T_{DIF} is the difference between the average temperature measured by the sensor and the thermal camera.

The temperature rises with an increase in load power, as illustrated in Figure 9. This is due to the increase in current flow through the IGBT module. It is evident that the temperature measurement by the sensor varies as the thermal gradients are non-uniform. This is caused by the fluctuations in the thermal spreading resistance, which rely on the IGBT's relative location and surface area in relation to the heatsink. FBG1 and FBG2 were positioned near the two IGBTs located at the center of the heatsink. Meanwhile, FBG3 was affixed to the densely packed rectifier positioned 52 mm away from the IGBTs.

Each sensor reading, T_{FBG1}, T_{FBG2}, and T_{FBG3}, is the average of three temperature measurements taken from each IGBT and rectifier on the heatsink, validating the potential of FBG array sensors for multipoint thermal sensing. Nonetheless, T_{DIF} is a result of

inherent errors within the spectrum analyzer, interface mismatch, and resistance within the tiny airgap across the IGBT–FBG interface.

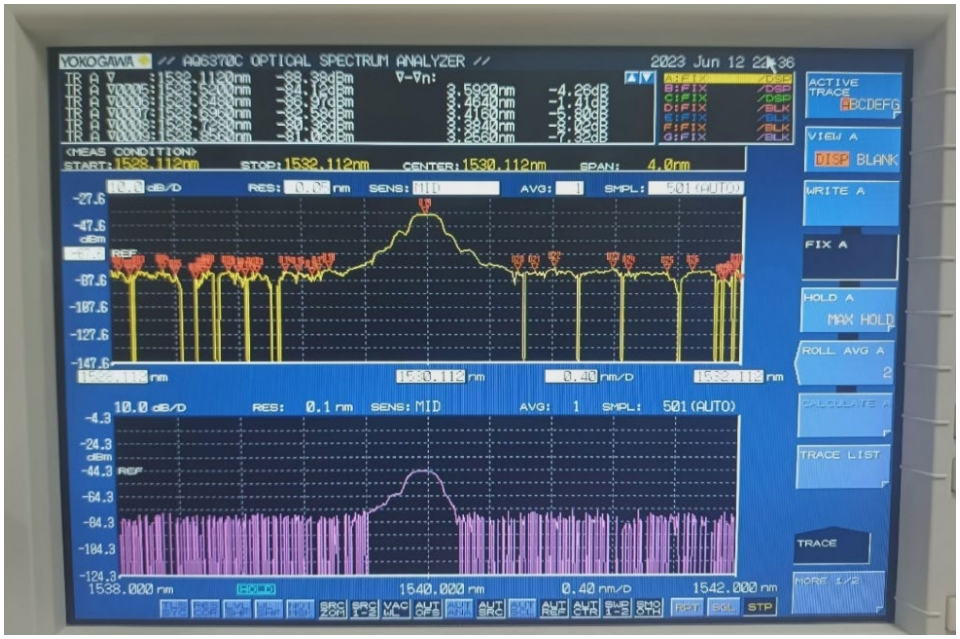

Figure 8. Observed reflection spectra for the FBG sensors on the optical spectrum analyzer.

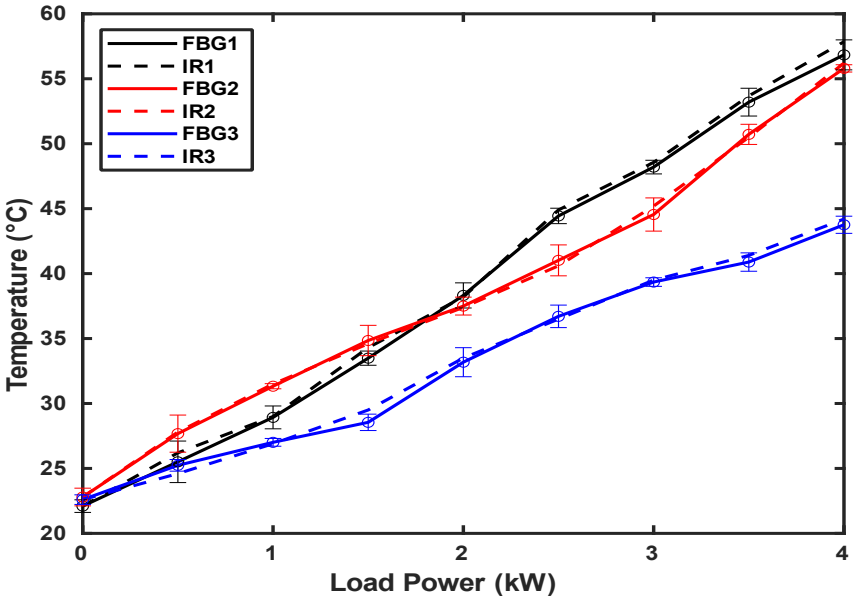

Figure 9. FBG temperature response to varying load power.

5.2. Effect of Airgap

A thermal pad with a conductivity of approximately 5.2 W/(mK) was inserted to minimize the temperature difference T_{DIF} resulting from the approximately 60 µm airgap between the temperature-sensitive part of the sensor and the baseplate and interface mismatch. This serves to occupy the airgap and enhance the heat transfer at the PSD's baseplate and FBG interface. The process employed to obtain the thermal profile of the IGBT in Figure 9 was replicated in Figure 10, which displays a noticeable enhancement in the precision of the sensor measurements since temperatures T_{FBG} and T_{IR} are closely correlated. The green line (FBG1) overlapped with the blue line (FBG2) as expected since

IGBT1 and IGBT2 have similar thermal profiles due to their parallel connection on a common heatsink in close proximity.

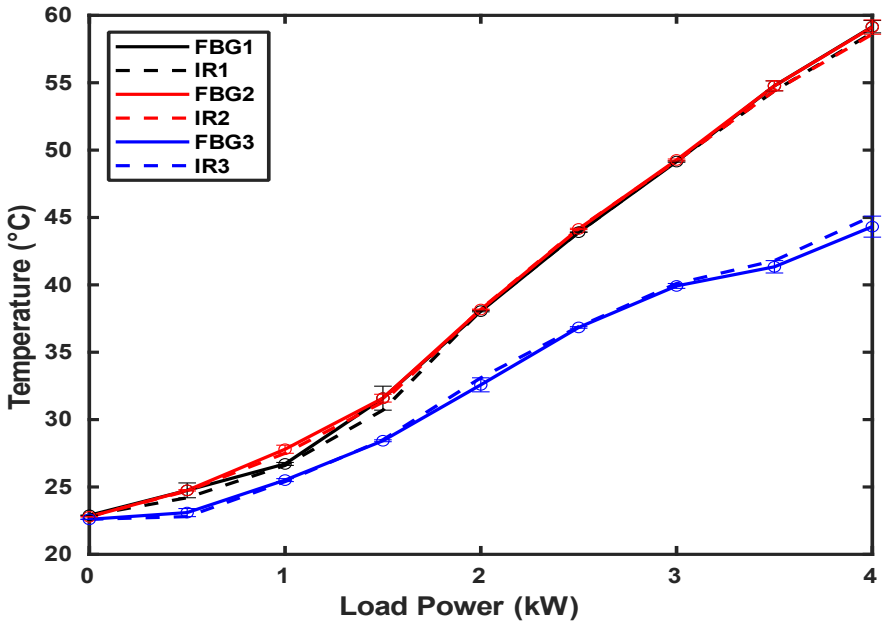

Figure 10. FBG temperature response to varying load power with minimized airgap effect.

In comparison to the previous measurement, a mean squared error of 0.37 was recorded. The fluctuation in the temperature curve of the IR camera and the estimated temperature of the FBG array demonstrate that the thermal gradient across the layer of the device is dependent upon P_L. The error bars provide a visual representation of the uncertainty in the measurements, with the maximum deviation of 1.54. This implies that the FBG sensor is a dependable technology for temperature distribution mapping in power electronic applications.

5.3. Prediction Using AI

The thermal imaging analysis of IGBTs plays a crucial role in predicting potential failures before they occur, leveraging the power of advanced artificial intelligence (AI) tools. These tools utilize neural networks (NNs) to process and interpret the thermal images captured from IGBTs under various operating conditions. By examining the heat distribution patterns, the NN is trained to recognize subtle anomalies that may indicate early signs of wear or damage.

In Figure 11, thermal images captured at two different time intervals are shown, providing a comparative view that helps in tracking the thermal behavior of the IGBT over time. Figure 11a shows a lower average temperature compared to Figure 11b. However, these differences are not easily discernible to the naked eye, making it challenging to identify areas that require attention. This comparison is crucial for understanding the development of potential issues. Figure 12 enhances this analysis by employing a neural network that identifies specific regions within the IGBT with abnormal heat signatures, highlighted as brighter areas in the image.

The NN architecture used in this work is similar to [23], with descending layers followed by ascending convolutional layers. The network contains skip connections in order to avoid the vanishing gradient problem. The dataset includes thermal images of IGBT modules captured under varying operating conditions. Labels indicating healthy and anomalous regions were provided by the domain experts. The network was trained on labeled datasets where areas of abnormal heating were annotated based on expert knowledge and physical inspections. A portion of the data was reserved for validation

to ensure generalization. Data augmentation techniques, such as rotation, flipping, and scaling, were applied to increase the diversity of the training samples. The network was trained using a supervised learning approach optimized for cross-entropy loss to classify regions as normal or anomalous. The output of the neural network was postprocessed (annotated) to generate the thermal map, as shown in Figure 12. The brighter areas (circled) in the image represent those regions where the neural network detected unusual thermal patterns. This visualization aids in identifying hotspots that may require further inspection. This approach not only enhances the accuracy of the damage prediction but also aids in proactive maintenance, ensuring the longevity and reliability of the IGBT components in various applications.

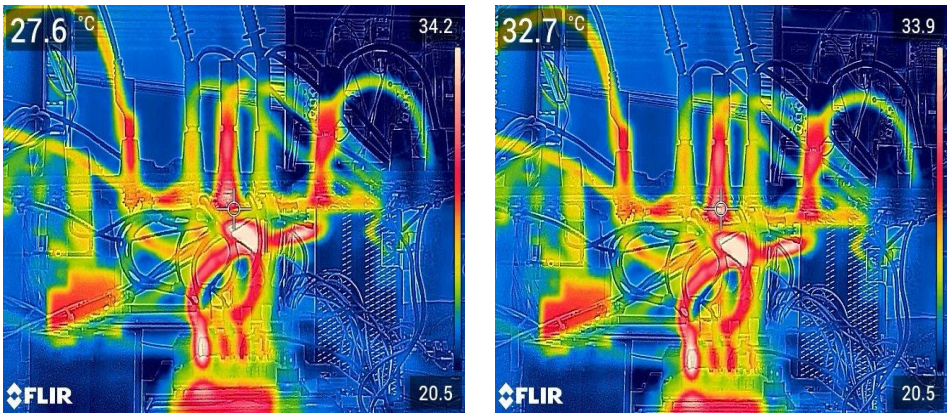

(**a**) (**b**)

Figure 11. (**a**) Thermal imaging of IGBT at time T1. (**b**) Thermal imaging of IGBT at time T2 (where T2 > T1).

Figure 12. Predictions of hotspots using neural networks.

6. Conclusions

This study examines the performance capabilities of multipoint FBG temperature sensing for IGBTs and other power semiconductor modules. A static thermal resistive network is employed to formulate the equivalent junction temperature of IGBT and rectifier modules, avoiding the need to dismantle the IGBT housing for sensor placement. The comparison between the air interface under study and the FBG–IGBT interface calibration indicates that the mechanical stress during its operation has not influenced the sensitivity of the sensors. Furthermore, the load power vs. temperature curve demonstrated the use of a single optical fiber with multiplexed sensor wavelengths for multipoint temperature sensing; this enables the comprehensive thermal profiling of the entire power system. The analysis of the airgap revealed that the FBG–IGBT sensor interface needed to be free of

an airgap or fitted with an appropriate thermal pad to enhance the temperature reading accuracy. Additionally, AI-powered neural networks processed thermal images of IGBTs to detect subtle heat anomalies, enabling predictive maintenance and improving component reliability. These findings were validated through experiments on a custom-built three-phase inverter system. In the future, a dedicated fiber sensing port could facilitate the integration of multiple FBG sensors into a distributed monitoring system. Furthermore, machine learning techniques can be employed to improve sensor calibration and accuracy by leveraging ambient temperature data and pre-trained models.

Author Contributions: Conceptualization, K.K.Q. and R.I.; methodology, R.I., K.K.Q., J.M. and M.A.; validation, R.I. and N.I.; formal analysis, R.I. and K.K.Q.; investigation, K.K.Q., N.I. and R.I.; resources, K.K.Q.; data curation, K.K.Q. and R.I.; writing—original draft preparation, R.I. and K.K.Q.; review and editing, K.K.Q., J.M. and N.I.; supervision, K.K.Q.; project administration, K.K.Q.; funding acquisition, K.K.Q. All authors have read and agreed to the published version of the manuscript.

Funding: This research was funded by DROC at KFUPM through grant no. ISP23219.

Institutional Review Board Statement: Not applicable.

Informed Consent Statement: Not applicable.

Data Availability Statement: The original contributions presented in the study are included in the article, further inquiries can be directed to the corresponding author.

Acknowledgments: Khurram Karim Qureshi would like to acknowledge the support provided by DROC at KFUPM through an outbound international visiting program (Project no. ISP23219).

Conflicts of Interest: The authors declare no conflicts of interest.

References

1. Xu, Z.; Jiang, D.; Li, M.; Ning, P.; Wang, F.F.; Liang, Z. Development of Si IGBT Phase-Leg Modules for Operation at 200 °C in Hybrid Electric Vehicle Applications. *IEEE Trans. Power Electron.* **2013**, *28*, 5557–5567. [CrossRef]
2. Liu, B.; Chen, G.; Lin, H.C.; Zhang, W.; Liu, J. Prediction of IGBT junction temperature using improved cuckoo search-based extreme learning machine. *Microelectron. Reliab.* **2021**, *124*, 114267. [CrossRef]
3. Zhang, J.; Du, M.; Jing, L.; Wei, K.; Hurley, W.G. IGBT Junction Temperature Measurements: Inclusive of Dynamic Thermal Parameters. *IEEE Trans. Device Mater. Reliab.* **2019**, *19*, 333–340. [CrossRef]
4. Luo, H.; Chen, Y.; Sun, P.; Li, W.; He, X. Junction Temperature Extraction Approach with Turn-Off Delay Time for High-Voltage High-Power IGBT Modules. *IEEE Trans. Power Electron.* **2016**, *31*, 5122–5132. [CrossRef]
5. Falck, J.; Andresen, M.; Liserre, M. Active thermal control of IGBT power electronic converters. In Proceedings of the IECON 2015—41st Annual Conference of the IEEE Industrial Electronics Society, Yokohama, Japan, 9–12 November 2015; IEEE: Piscataway, NJ, USA; Volume 000001, pp. 1–6.
6. Chen, G.; Han, D.; Mei, Y.-H.; Cao, X.; Wang, T.; Chen, X.; Lu, G.-Q. Transient Thermal Performance of IGBT Power Modules Attached by Low-Temperature Sintered Nanosilver. *IEEE Trans. Device Mater. Reliab.* **2012**, *12*, 124–132. [CrossRef]
7. Sathik, M.H.M.; Pou, J.; Prasanth, S.; Muthu, V.; Simanjorang, R.; Gupta, A.K. Comparison of IGBT junction temperature measurement and estimation methods—A review. In Proceedings of the 2017 Asian Conference on Energy, Power and Transportation Electrification (ACEPT 2017), Singapore, 24–26 October 2017; pp. 1–8. [CrossRef]
8. Sathik, M.; Jet, T.K.; Gajanayake, C.J.; Simanjorang, R.; Gupta, A.K. Comparison of power cycling and thermal cycling effects on the thermal impedance degradation in IGBT modules. In Proceedings of the IECON 2015—41st Annual Conference of the IEEE Industrial Electronics Society, Yokohama, Japan, 9–12 November 2015; pp. 1170–1175.
9. Almubarak, A.A. The Effects of Heat on Electronic Components. *Int. J. Eng. Res. Appl.* **2017**, *07*, 52–57. [CrossRef]
10. Choi, U.-M.; Blaabjerg, F. Separation of Wear-Out Failure Modes of IGBT Modules in Grid-Connected Inverter Systems. *IEEE Trans. Power Electron.* **2018**, *33*, 6217–6223. [CrossRef]
11. Isa, R.; Mirza, J.; Ghafoor, S.; Mustafa Khan, M.Z.; Qureshi, K.K. Junction Temperature Optical Sensing Techniques for Power Switching Semiconductors: A Review. *Micromachines* **2023**, *14*, 1636. [CrossRef] [PubMed]
12. Avenas, Y.; Dupont, L. Evaluation of IGBT thermo-sensitive electrical parameters under different dissipation conditions—Comparison with infrared measurements. *Microelectron. Reliab.* **2012**, *52*, 2617–2626. [CrossRef]
13. Blackburn, D.L. Temperature measurements of semiconductor devices—A review. In Proceedings of the Annual IEEE Semiconductor Thermal Measurement and Management Symposium, San Jose, CA, USA, 11 March 2004; Volume 20, pp. 70–80.
14. Kim, M.K.; Yoon, Y.D.; Yoon, S.W. Actual Maximum Junction Temperature Estimation Process of Multichip SiC MOSFET Power Modules with New Calibration Method and Deep Learning. *IEEE J. Emerg. Sel. Top. Power Electron.* **2022**, *11*, 5602–5612. [CrossRef]

15. Wang, X.; Zhu, C.; Luo, H.; Lu, Z.; Li, W.; He, X.; Ma, J.; Chen, G.; Tian, Y.; Yang, E. IGBT junction temperature measurement via combined TSEPs with collector current impact elimination. In Proceedings of the ECCE 2016—IEEE Energy Conversion Congress and Exposition, Milwaukee, WI, USA, 18–22 September 2016; pp. 1–6.
16. Isa, R.; Abido, M.; Qureshi, K.K. Junction Temperature Measurement in High Power Electronic Applications Using Fiber Bragg Grating-based Sensors. In Proceedings of the 28th International Conference on Optical Fiber Sensors, ACT CITY, Hamamatsu, Japan, 20–24 November 2023; Optica Publishing Group: Washington, DC, USA, 2023; p. W4.34.
17. Bryant, A.; Yang, S.; Mawby, P.; Xiang, D.; Ran, L.; Tavner, P.; Palmer, P.R. Investigation Into IGBT dV/dt During Turn-Off and Its Temperature Dependence. *IEEE Trans. Power Electron.* **2011**, *26*, 3019–3031. [CrossRef]
18. Bęczkowski, S.; Ghimre, P.; de Vega, A.R.; Munk-Nielsen, S.; Rannestad, B.; Thøgersen, P. Online Vce measurement method for wear-out monitoring of high power IGBT modules. In Proceedings of the 2013 15th European Conference on Power Electronics and Applications (EPE), Lille, France, 2–6 September 2013; pp. 1–7.
19. Kim, Y.-S.; Sul, S.-K. On-line estimation of IGBT junction temperature using on-state voltage drop. In Proceedings of the Conference Record of 1998 IEEE Industry Applications Conference, Thirty-Third IAS Annual Meeting (Cat. No. 98CH36242), St. Louis, MO, USA, 12–15 October 1998; Volume 2, pp. 853–859.
20. Motto, E.R.; Donlon, J.F. IGBT module with user accessible on-chip current and temperature sensors. In Proceedings of the 2012 Twenty-Seventh Annual IEEE Applied Power Electronics Conference and Exposition (APEC), Orlando, FL, USA, 5–9 February 2012; pp. 176–181.
21. Wang, R.; Sabate, J.; Mainali, K.; Sadilek, T.; Losee, P.; Singh, Y. SiC Device Junction Temperature Online Monitoring. In Proceedings of the 2018 IEEE Energy Conversion Congress and Exposition (ECCE 2018), Portland, OR, USA, 23–27 September 2018; pp. 387–392.
22. Zarebski, J.; Górecki, K.; Bisewski, D. A New Electrothermal Model of the Power MOSFET for SPICE. In Proceedings of the 11th International Conference Mixed Design of Integrated Circuits and Systems, Szczecin, Poland, 24–26 June 2004; pp. 1–5.
23. Chen, S.; Vilchis-Rodriguez, D.; Djurovic, S.; Barnes, M.; McKeever, P.; Jia, C. FBG Head Size Influence on Localized On-Chip Thermal Measurement in IGBT Power Modules. *IEEE Sens. J.* **2022**, *22*, 21684–21693. [CrossRef]
24. Wang, Y.; Taylor, P.; Simpson, R.A.; Tarr, C.; Nicholson, M.; Bell, D.; Sun, T.; Grattan, K.T.V.; Fabian, M.; Ribeiro, B.C.R. Semiconductor Device. WO 2022/223101 A1, 27 October 2022.
25. Vestas Wind System. Optical Sensor System and Detecting Method for an Enclosed Semiconductor Device Module. U.S. Patent 2011/0267598 A1, 3 November 2011.
26. Siemens. Assembly Consisting of Electronic Components and Comprising a Temperature Sensor. WO 2001/71301 A1, 27 September 2001.
27. Chen, S.; Vilchis-Rodriguez, D.; Barnes, M.; Djurovic, S. Direct On-chip IGBT Thermal Sensing using Adhesive bonded FBG Sensors. *IEEE Sens. J.* **2023**, *23*, 22507–22516. [CrossRef]
28. He, J.; Xu, B.; Xu, X.; Liao, C.; Wang, Y. Review of Femtosecond-Laser-Inscribed Fiber Bragg Gratings: Fabrication Technologies and Sensing Applications. *Photonic Sens.* **2021**, *11*, 203–226. [CrossRef]
29. Drexhage, P.; Wintrich, A. Calculating Junction Temperature Using a Module Temperature Sensor. 2020. Available online: https://www.semikron-danfoss.com/service-support/downloads/detail/semikron-application-note-calculating-junction-temperature-using-a-module-temperature-sensor-en-2020-01-29-rev-02.html (accessed on 2 June 2024).
30. SEMIKRON. Power Semiconductors Discrets and Stacks. 2019. Available online: https://www.semikron.com/products/product-lines/discrete-diodes-thyristors.html (accessed on 20 June 2024).
31. Chen, S.; Vilchis-Rodriguez, D.; Djurovic, S.; Barnes, M.; McKeever, P.; Jia, C. Direct on Chip Thermal Measurement in IGBT Modules Using FBG Technology—Sensing Head Interfacing. *IEEE Sens. J.* **2022**, *22*, 1309–1320. [CrossRef]